Research Paper

Fatigue design of a mechanically biocompatible lattice for a proof-of-concept femoral stem

Sajad Arabnejad Khanoki, Damiano Pasini*,[1]

Mechanical Engineering Department, McGill University Montreal, QC, Canada H3A 2K6

ARTICLE INFO

ABSTRACT

A methodology is proposed to design a spatially periodic microarchitectured material for a two-dimensional femoral implant under walking gait conditions. The material is composed of a graded lattice with controlled property distribution that minimizes concurrently bone resorption and interface failure. The periodic microstructure of the material is designed for fatigue fracture caused by cyclic loadings on the hip joint as a result of walking. The bulk material of the lattice is Ti6AL4V and its microstructure is assumed free of defects. The Soderberg diagram is used for the fatigue design under multiaxial loadings. Two cell topologies, square and Kagome, are chosen to obtain optimized property gradients for a two-dimensional implant. Asymptotic homogenization (AH) theory is used to address the multiscale mechanics of the implant as well as to capture the stress and strain distribution at both the macro and the microscale. The microstress distribution found with AH is also compared with that obtained from a detailed finite element analysis. For the maximum value of the von Mises stress, we observe a deviation of 18.6% in unit cells close to the implant boundary, where the AH assumption of spatial periodicity of the fluctuating fields ceases to hold.

In the second part of the paper, the metrics of bone resorption and interface shear stress are used to benchmark the graded cellular implant with existing prostheses made of fully dense titanium implant. The results show that the amount of initial postoperative bone loss for square and Kagome lattice implants decreases, respectively, by 53.8% and 58%. In addition, the maximum shear interface failure at the distal end is significantly reduced by about 79%.

A set of proof-of-concepts of planar implants have been fabricated via Electron Beam Melting (EBM) to demonstrate the manufacturability of Ti6AL4V into graded lattices with alternative cell size. Optical microscopy has been used to measure the morphological parameters of the cellular microstructure, including cell wall thickness and pore size, and compared them with the nominal values. No sign of fracture or incomplete cell walls was observed, an assessment that shows the satisfactory metallurgical bond of cell walls and the structural integrity of the implants.

1. Introduction

An orthopaedic hip implant is expected to support dynamic forces generated by human activities. To avoid progressive and localized damage caused by daily cyclic loading, the prosthesis is to be designed for fatigue under high cycle regime. Recently, a methodology has been developed to design a novel hip implant made of a cellular material with a periodic microarchitecture (Khanoki and Pasini, 2012). In

---

*Corresponding author. Tel.: +1 514 398 6295; fax: +1 514 398 7365.
  E-mail addresses: sajad.arabnejadkhanoki@mail.mcgill.ca (S. Arabnejad Khanoki), Damiano.pasini@mcgill.ca (D. Pasini).
  [1]Present address: Room 372, MacDonald Engineering Building, Mechanical Engineering Department, McGill University, Montreal, QC, Canada H3A 2K6.

contrast to current hip replacement implants typically made out of a fully solid material which can be coated with a porous layer, this implant is completely porous with a lattice microstructure displaying graded property distribution. The advantage of controlling the microarchitecture is twofold. First, the overall implant can be designed to be more compliant, which reduces stress shielding and bone resorption (Behrens et al., 2008; Glassman et al., 2006; Huiskes et al., 1992; Pettersen et al., 2009). Second, the material porosity can be optimized to also reduce bone-implant interface stresses, thereby lowering implant micromotion. Although encouraging, these results have been obtained by applying a static loading regime to the implant, thus neglecting the impact of cyclic loading that generally boosts the risk of fatigue failure.

In literature, there are several experimental and numerical studies focusing on the fatigue analysis of hip implants (Baleani et al., 1999; Hedia et al., 1996; Kayabasi and Ekici, 2007; Li et al., 2002; Nganbe et al., 2011; Ploeg et al., 2009; Raimondi and Pietrabissa, 1999; Senalp et al., 2007). For example, fatigue loading conditions, ISO 7206/3, have been applied to a hip stem to predict its elastic stress via large deflection finite element analysis (Ploeg et al., 2009). It has been demonstrated via experiments that the high cycle fatigue-life of hip stems can be adequately predicted by using alternative fatigue theories, such as Morrow, Smith–Watson–Topper (SWT), and Goodman. The Soderberg theory has also been used to design a cemented implant for infinite life; the results have been proved to be accurate although more conservative than those obtained with Goodman and Gerber theories (Hedia et al., 1996; Kayabasi and Ekici, 2007).

Among the biocompatible materials used for reconstructive orthopaedics, porous tantalum has been recently proved to be effective in facilitating bone ingrowth. For this reason, porous tantalum has been lately the object of studies aiming at characterizing its fatigue fracture mechanisms (Sevilla et al., 2007; Zardiackas et al., 2001). Similar to open cellular foams, porous tantalum has a random cellular microstructure which is typically imparted by the manufacturing process, involving a chemical deposition of pure tantalum on carbon skeleton (Bobyn et al., 2004; Murr et al., 2010, 2009). Due to its pore structure, the fracture propagation of porous tantalum under fatigue has been observed similar to that of open-cell foams (Sevilla et al., 2007; Zardiackas et al., 2001; Zhou and Soboyejo, 2004). It has been observed that the bending dominated failure mode of the unit cell (Gibson, 2005; Liu and Du, 2011; Vigliotti and Pasini, 2012) at the cell joints nucleates cracks that propagate throughout a strut until the final break (Li et al., 2012; Sevilla et al., 2007; Zardiackas et al., 2001). The joints are indeed the weakest parts of a cellular material, because stress peaks localize in those regions and thus severely reduce fatigue strength. However, if the geometry of the cell joints, i.e. the locations where the struts converge, is designed to level out any curvature discontinuity (Abad et al., 2012), then the joint strength can be significantly increased, thereby improving the fatigue strength of the cellular material.

While several analytic methods have been proposed to study the fatigue life of cellular structures (Cote et al., 2006; Côté et al., 2007a, 2007b; Huang and Liu, 2001a, b; Huang and Lin, 1996; Olurin et al., 2001), the majority fail to accurately capture the real stress distribution generated in the lattice cells (Simone and Gibson, 1998). To overcome this problem, more recently a fatigue design methodology has been introduced to model the elastic–plastic behavior of cellular materials, and used to generate fatigue design diagrams for cellular materials (Abad et al., 2012). The method focuses on uni-axial and shear loading for relative density $\rho \leq 0.3$.

In this paper, the method of Abad et al. (2012) is first extended to account for multiaxial loadings of cellular materials under infinite fatigue life. The approach is then applied to the fatigue design of a planar proof-of-concept hip implant that is loaded under cycling forces of walking. Two representative cell topologies are selected to design the hip implant: the square lattice, which is a bending dominated behaviour, and the Kagome cell, whose main deformation is caused by the strut stretching. The results obtained in this paper are numerically verified through the multilevel method for damage analysis (Ghosh et al., 2001; Raghavan and Ghosh, 2004). The performance of the two lattice implants is compared in terms of bone resorption, interface stress, and mechanical strength. Finally, 2D proof-of-concepts of graded cellular implants with a square cell are fabricated to assess the manufacturability of the lattice microarchitecture.

2. Fatigue analysis of cellular materials

The deformation and failure mechanisms of a structure with heterogeneous material can occur at both macro and microscopic length scales. Experimental studies have shown that a cellular material under repetitive loading develop cracks at the microscale in regions with high stress concentration, from which fracture propagates throughout the strut cross sections (Sevilla et al., 2007; Zardiackas et al., 2001; Zhou and Soboyejo, 2004). Since the micromechanisms of deformation and fracture play a crucial role in the fatigue resistance of a cellular material, it is essential in the design of a cellular component to capture and account for the microscopic stress and strain distribution. Here, we resort to Asymptotic Homogenization (AH) theory to determine the homogenized properties of the cellular material and capture the microscopic stress and strain distribution via the analysis of a representative volume element (RVE). The underlying assumption of AH is the periodicity of RVE and field quantities at macro and microscopic scales. AH method has been widely used in multiscale analysis of composite materials (Kalamkarov et al., 2009; Kanouté et al., 2009), topology optimization (Bendsøe and Kikuchi, 1988; Bendsøe and Sigmund, 2003; Díaaz and Kikuchi, 1992; Guedes and Kikuchi, 1990; Hassani and Hinton, 1998; Suzuki and Kikuchi, 1991), and hierarchical design of materials and structures (Coelho et al., 2008, 2011; Gonçalves Coelho et al., 2011; Rodrigues et al., 2002).

Recently, AH has been also used to propose a computational procedure for the fatigue design of periodic cellular materials (Abad et al., 2012). Yield and ultimate strength of lattice materials have been determined for relative density $\rho \leq 0.3$, and used to construct modified Goodman diagrams of selected lattices under uni-axial and shear loading. This method is here extended to construct the Soderberg fatigue diagram for fatigue failure analysis of cellular structures under multiaxial loading conditions for the whole range of relative density. Here, we assume the specimen to be free of defects, such as scratches, notches and nicks. As a result, the constant life diagram can be constructed for the design of the material against fatigue failure (Nicholas and Zuiker, 1989). The damage-free assumption of the microstructure would also ensure the validity of the periodicity assumption of the microstructure. As a result, AH theory can be used to capture the stress distribution within the unit cell. To account for the effect of micro-defects on the

fatigue fracture of the material microstructure, computational techniques, such as the multilevel computational approach (Ghosh et al., 2001; Raghavan and Ghosh, 2004) or the mesh superposition method (Takano et al., 2003), can be included in the method to model local defects explicitly. This work is beyond the scope of this paper and thus is left to future study.

To obtain the stress distribution within the unit cell through AH, the following local problem defined on the RVE should be solved (Guedes and Kikuchi, 1990; Hollister and Kikuchi, 1992):

$$\int_{Y_C} E_{ijpm}\varepsilon_{ij}^1(v)\varepsilon_{pm}^{*kl}(u)dY = \int_{Y_C} E_{ijkl}\varepsilon_{ij}^1(v)\overline{\varepsilon}_{kl}dY \tag{1}$$

where $\varepsilon_{ij}^1(v)$ is the virtual strain, $\varepsilon_{ij}^{*kl}(u)$ is the microstructural strain corresponding to the component kl of the macroscopic strain tensor $(\overline{\varepsilon}_{kl})$, Y_c is the solid part of the cell, and E_{ijkl} is the local elasticity tensor. The periodicity of field quantities at the microscale is ensured by imposing periodic boundary conditions on the RVE edges; hence the nodal displacements on the opposite edges are set to be equal (Hassani, 1996; Hollister and Kikuchi, 1992). Considering the assumption of small deformation and elastic material behavior, the solution of Eq. (1) leads to a linear relation between the macroscopic $(\overline{\varepsilon}_{ij})$ and microscopic (ε_{ij}) strain through the local structural tensor M_{ijkl}:

$$\varepsilon_{ij} = M_{ijkl}\overline{\varepsilon}_{kl}, M_{ijkl} = \frac{1}{2}(\delta_{ik}\delta_{jl} + \delta_{il}\delta_{jk}) - \varepsilon_{ij}^{*kl} \tag{2a, b}$$

where δ_{ij} is the Kronecker delta. For a two-dimensional case, three independent unit strains are required to construct the M_{ijkl} matrix. The effective stiffness tensor E_{ijkl}^H is then calculated by the following equation:

$$E_{ijkl}^H = \frac{1}{|Y|}\int_{Y_C} E_{ijpm}M_{pmkl}dY \tag{3}$$

where $|Y|$ is the volume of the entire unit cell with voids. The homogenized stiffness matrix relates the macroscopic strains to the macroscopic stresses of the homogenized material. Once the local structure tensor, M_{ijkl}, is obtained, the microscopic stresses corresponding to the macroscopic strain can be obtained via the following equation:

$$\sigma_{ij} = E_{ijkl}M_{klmn}\overline{\varepsilon}_{mn} \tag{4}$$

Using the homogenized stiffness matrix, the microscopic stress distribution σ_{ij} can, therefore, be related to the multiaxial macroscopic stress $\overline{\sigma}_{ij}$ by the following relation:

$$\sigma_{ij} = E_{ijkl}M_{klmn}(E_{rsmn}^H)^{-1}\overline{\sigma}_{rs} \tag{5}$$

The von Mises stress distribution over the microstructure is then used to capture the yield surface of the unit cell expressed as follow:

$$\overline{\sigma}_{ij}^y = \frac{\sigma_{ys}}{max\{\sigma_{vM}(\overline{\sigma}_{ij})\}}\overline{\sigma}_{ij} \tag{6}$$

where $\overline{\sigma}_{ij}^y$ is the yield surface of the unit cell, σ_{ys} is the yield strength of the bulk material, and $\sigma_{vM}(\cdot)$ is the von Mises stress of the microstructure corresponding to the applied macroscopic stress. The fatigue surface of the unit cell can be obtained through the product of the unit cell yield strength with the ratio of the

endurance limit and yield strength of the bulk material as:

$$\overline{\sigma}_{ij}^e = \overline{\sigma}_{ij}^y \frac{\sigma_{es}}{\sigma_{ys}} \tag{7}$$

where $\overline{\sigma}_{ij}^e$ is the endurance limit of the unit cell and σ_{es} is the endurance limit of the bulk material. These properties are required to construct the Soderberg fatigue diagram under multiaxial loading condition:

$$\frac{\overline{\sigma}_{ij}^m}{\overline{\sigma}_{ij}^y} + \frac{\overline{\sigma}_{ij}^a}{\overline{\sigma}_{ij}^e} = \frac{1}{SF} \tag{8}$$

where the mean and alternating macroscopic stresses, respectively, $\overline{\sigma}_{ij}^m$ and $\overline{\sigma}_{ij}^a$ are calculated by the following relations:

$$\overline{\sigma}_{ij}^m = \frac{\overline{\sigma}_{ij}^{max} + \overline{\sigma}_{ij}^{min}}{2}, \overline{\sigma}_{ij}^a = \frac{\overline{\sigma}_{ij}^{max} - \overline{\sigma}_{ij}^{min}}{2} \tag{9a, b}$$

$\overline{\sigma}_{ij}^{max}$ and $\overline{\sigma}_{ij}^{min}$ are the multiaxial macroscopic stresses that cause, respectively, the highest and the lowest values of the von Mises stress in the microstructure.

In this study, the above procedure is applied to design a 2D graded cellular implant. To generate the lattice, we select the square and Kagome unit cells, as representative of bending and stretching dominated topologies, and we predict their mechanical and fatigue properties. For the material properties of the lattice, we consider Ti6Al4V (Parthasarathy et al., 2010) with mechanical properties: 900 MPa for the yield strength of the solid material, 600 MPa for the fatigue strength at 10^7 cycles, 120 GPa for the Young's modulus, and 0.3 for the Poisson's ratio. These properties are experimental values obtained from mechanical testing of EBM samples after postprocess by hot-isostatic-pressing (HIP) (ARCAM, 2013). Although micro defects and voids can be largely eliminated by the HIP process, remnants may still persist in built samples. In our analysis, we assumed that the specimen is free of micro defects, and the cell wall material is a continuum medium with properties comparable to those of the bulk material.

For long terms applications of Ti6Al4V, concerns on the toxic effect of vanadium and aluminum have led to the development of a second generation of titanium alloys with nontoxic alloying elements, such as Ta, Nb, Zr (Geetha et al., 2009; Schuh et al., 2007). While we acknowledge this advance, in this exploratory study we select Ti6Al4V because it is the most common titanium alloy used with EBM (Li et al., 2012, 2010; Marin et al., 2010; Murr et al., 2010, 2012, 2009). In addition, the mechanical properties of Ti6Al4V including elastic Young's modulus, yield, ultimate and fatigue strength, are well documented in the literature for lattice samples fabricated by EBM, (Li et al., 2012; Murr et al., 2010, 2012, 2009; Parthasarathy et al., 2010). These experimental data provide reference values to verify the results of this work.

2.1. Prediction of the effective mechanical properties of the unit cell

The effective elastic moduli and yield surfaces of square and Kagome lattices, with uniform wall thickness, are obtained by using AH for the range of relative density $0.05 \leq \rho \leq 1$. Fig. 1 illustrates the homogenized elastic constants of the cell topologies as a function of relative density. As can be seen, the effective Young's modulus, shear modulus, and Poisson's ratios converge to the elastic constants of the base solid material as the relative density reaches one. Since the Kagome cell topology is elastically
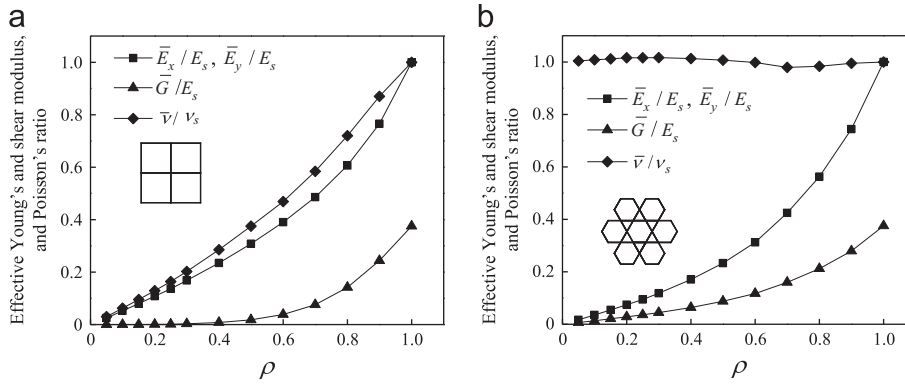
Fig. 1 – Effective elastic constants as a function of relative density for the (a) square and (b) Kagome lattices.

isotropic and the square has orthotropic symmetry, the Young's modulus is equal in both x and y directions. The square cell has a superior elastic stiffness due to the capacity of realigning the cell walls along the loading direction, but it exhibits very low stiffness under shear loading as a result of cell wall bending.

The yield surfaces of the cell topologies are also obtained for multiaxial macroscopic stresses. As shown in Eq. (6) and being in linear elasticity, the location of the yield point on the yield surface of each lattice is obtained by multiplying the macroscopic stress with the ratio of the material yield strength and the maximum von Mises stress. Figs. 2 and 3 show the yield surfaces normalized with respect to the yield strength of the square and Kagome lattices in the uniaxial and shear loading directions at a given relative density. Fig. 2 refers to the square lattice for the relative density of 50%, and Fig. 3 pertains to the Kagome cell for the relative density of 30%. We selected 30% for the Kagome, because for a 50% relative density the base material almost completely fills the triangular voids, and thus the Kagome structure cannot be realized.

Once the yield surface is determined, the multiaxial endurance limit of the cell can be obtained by scaling the yield surface with the coefficient given in Eq. (7). These data can be inserted into Eq. (8) for the infinite-life design of cellular structures under multi-axial fatigue loading conditions. For design purposes, it is often convenient to resort to closed-form expressions that can approximately describe the geometry of a yield surface. For this reason, Table 1 lists the functions along with relative fitting parameters of the yield surfaces for the unit cells here under investigation. For the square cell (Fig. 2b), a pyramid with an elliptical base is used to resemble the yield surface. F_{xy}^* (Table 1) governs both the slenderness ratio and the inclination of the major axis of the elliptical base. For the Kagome cell (Fig. 3b), the yield surface is approximated by a parallelogram, and m_1 and m_2 (Table 1) are the slopes of the parallelogram lines, expressed as a function of the relative density. The parameters $\overline{\sigma}_{xx}^y$, $\overline{\sigma}_{yy}^y$, $\overline{\tau}_{xy}^y$ (Table 1) are the yield strength of the unit cell under uni-axial and shear stresses. Fig. 4a and b show the variation of the yield strength as a function of relative density. When the material is fully dense, the yield strength is equal to that of its solid material. A common feature in the plots of Fig. 4 is the abrupt decrease of the effective yield strength for decreasing values of relative density. The reason for this is the presence of stress concentration at the cell joints, which locally increases the level of stress. We note here that the fatigue strength of the lattice can be

significantly improved by optimizing the cell shape and removing the curvature discontinuity at the joints (Abad et al., 2012).

3. Fatigue design of a hip implant with controlled lattice microarchitecture

Fig. 5 illustrates the methodological steps to design a graded cellular implant for infinite fatigue life. The approach combines multiscale mechanics and multiobjective optimization. The former deals with the scale-dependent material structure, where the local problem of the RVE is first solved, and then the effective elastic moduli and yield strength are obtained and used as homogenized properties of the macroscopic model of the implant. The latter handles the conflicting nature of bone resorption and implant interface stress. A fatigue failure theory can thus be embedded in the procedure to design the implant for infinite fatigue life. A brief description of the main steps identified by the numbers in the flowchart is given in Fig. 5.

- (1) A finite element model of the bone is created by processing CT-scan data of a patient bone.
- (2) A 3D lattice microstructure is considered as the building block of the implant, and its mechanical properties are predicted through AH. The homogenized elastic modulus, yield and fatigue surfaces of the cell topology under multiaxial loading conditions are obtained.
- (3, 4) From FEA, the mean and alternative macroscopic stresses are obtained, and used in the fatigue design diagram to determine the design safety factor (SF). In this study, the Soderberg's fatigue failure criterion is considered for the analysis.
- (5) The two conflicting objective functions, bone resorption $m_r(\mathbf{b})$ and interface failure index $F(\mathbf{b})$, are minimized via a multiobjective optimization strategy subjected to a set of inequality constraints. The amount of bone resorption is determined by comparing the local strain energy per unit of bone mass between the preoperative and the postoperative situation. Bone start to lose mass when its local strain energy (U_i) per unit of bone mass (ρ), averaged over n loading cases ($S = ((1/n)\Sigma_{i=1}^n U_i/\rho)$), is beneath the local reference value $(1-s)S_{ref}$. S_{ref} is the value of S when no prosthesis is present, and s is the threshold level or dead zone that bone can tolerate
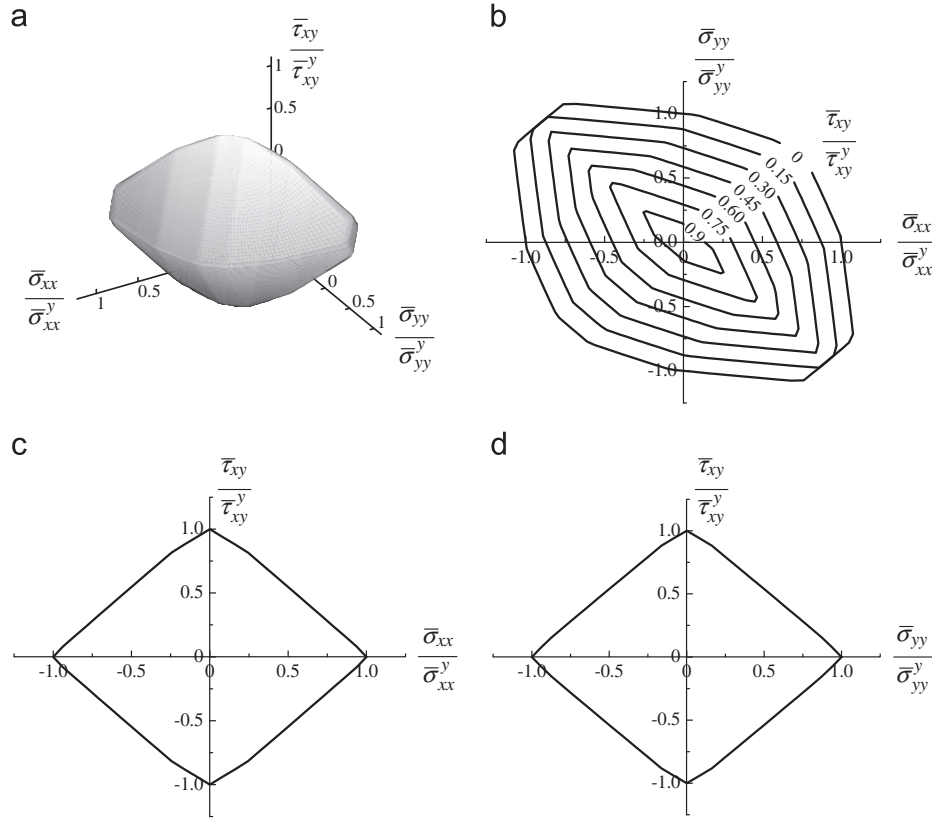
Fig. 2 – Yield surface of a square cell topology under combined multiaxial macroscopic stress state ($\bar{\sigma}_{xx}$, $\bar{\sigma}_{yy}$ and $\bar{\tau}_{xy}$) for a relative density $= 50\%$.

before resorption. Using this definition, the fraction m_r of resorbed bone mass can be obtained from:

$$m_r(\mathbf{b}) = \frac{1}{M} \int_V g(S(\mathbf{b}))\rho\, dV \tag{10}$$

where M and V are the original bone mass and volume, respectively, and $g(S(\mathbf{b}))$ is a resorptive function equal to unity if the local value of S is beneath the local value of $(1-s)S_{ref}$ and equal to 0 if $(1-s)S_{ref} < S$. In this study, 0.5 is the value assumed for the dead zone s (Kuiper and Huiskes, 1992). The interface failure index $F(\mathbf{b})$ is expressed by the following relation:

$$F(\mathbf{b}) = max\left\{ \frac{f(\sigma)_i}{\frac{1}{A}\int_A f(\sigma)_i}\, dA \right\} \tag{11}$$

where i is the loading case (1–3), and A is the interface area. $f(\sigma)$ is defined as the interface failure caused by shear stress, and is expressed as τ/S_s, where τ is the local shear stress at the bone-implant interface, and S_s is the bone shear strength. In Eq. (11), the interface failure $f(\sigma)$ is normalized with its average over the bone-implant interface area. The minimization of $F(\mathbf{b})$ will lead to a design with minimum and uniform shear stress distribution at the interface. The shear strengths of bone can be expressed as a function of bone apparent density according to the power law relation obtained by Pal et al. (2009):

$$S_s = 21.6\rho^{1.65} \tag{12}$$

During the optimization procedure, the values of mean porosity and pore size are selected to ensure bone ingrowth (Bragdon et al., 2004; Harrysson et al., 2008), and the minimum thickness of the cell walls is determined by the resolution of the manufacturing process, i.e. the manufacturing limits.

- (6) The vector $\boldsymbol{b}$ of the design variables is updated until the set of non-dominated solutions of the Pareto front are obtained.

The methodology described above is now applied for the design of a 2D graded cellular implant. Square and Kagome cell topologies, which are characterized in the previous section, are considered as the cell architecture of the implant. The lattice is designed to support the cyclic load of walking and is optimized to reduce bone resorption and interface stress. The FEA model of the femur and implant, loading and boundary conditions, and the results are described in the following sections.

4. Design of a 2D femoral implant with a graded cellular material

4.1. 2D FEM model of the femur

Fig. 6a shows the geometry of the femur considered in this work along with the applied loads and boundary conditions. CT scan data of a 38-year-old male, obtained through the visible human project (VHP) database of the national library of medicine (NLM, USA), is used to construct the 3D model of the femur. The stack of CT images are imported into ITK-SNAP (Yushkevich et al., 2006) to
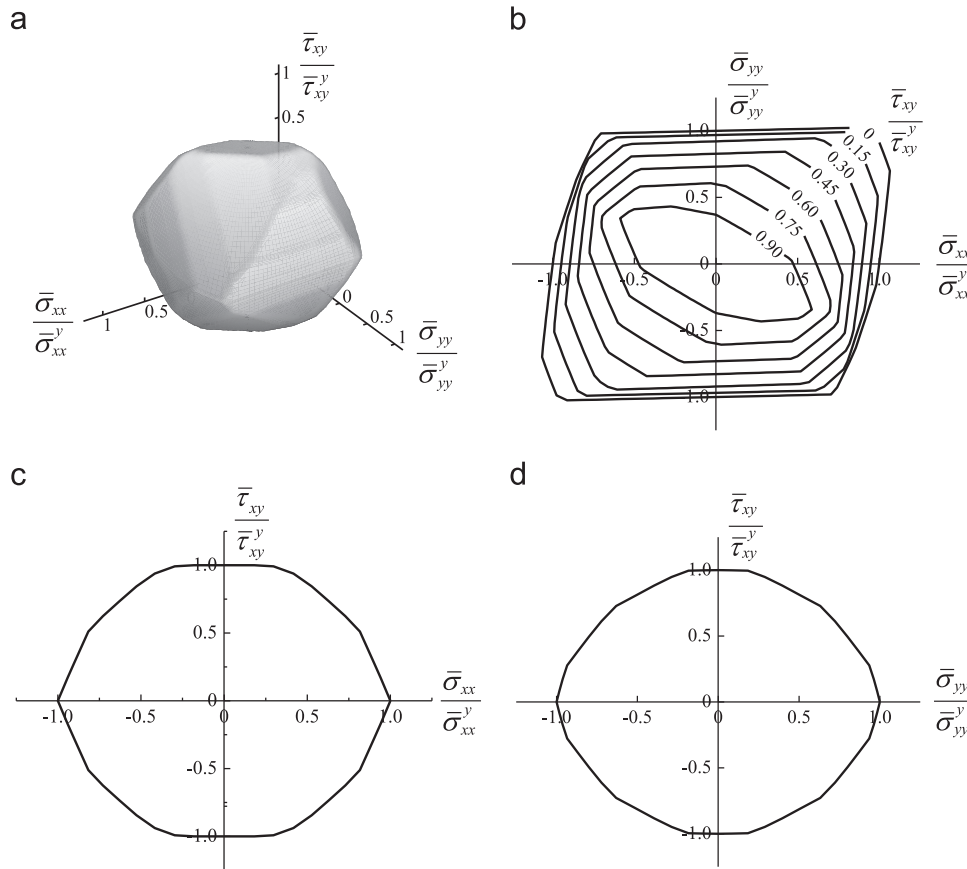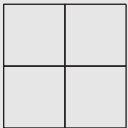
a

b

c

d

Fig. 3 – Yield surface of a Kagome cell topology under combined multiaxial macroscopic stress state ($\bar{\sigma}_{xx}$, $\bar{\sigma}_{yy}$ and $\bar{\tau}_{xy}$) for a relative density $=30\%$.

Table 1 – Yield surfaces as a function of relative density for square and Kagome unit cells.		
	Yield function	Constant
	$\left(\dfrac{\bar{\sigma}_{xx}}{\bar{\sigma}_{xx}^{y}}\right)^2 + 2F_{xy}^*\left(\dfrac{\bar{\sigma}_{xx}}{\bar{\sigma}_{xx}^{y}}\right)\left(\dfrac{\bar{\sigma}_{yy}}{\bar{\sigma}_{yy}^{y}}\right) + \left(\dfrac{\bar{\sigma}_{yy}}{\bar{\sigma}_{yy}^{y}}\right)^2 = \left(\dfrac{\bar{\tau}_{xy}}{\bar{\tau}_{xy}^{y}}-1\right)^2$	$F_{xy}^* = -1.6787\rho^2 + 2.539\rho - 0.42$
	$max\left\{\begin{array}{l} \left\lvert\dfrac{\bar{\sigma}_{xx}}{\bar{\sigma}_{xx}^{y}} - \dfrac{\bar{\sigma}_{yy}}{m_1\bar{\sigma}_{yy}^{y}}\right\rvert - \left(1 - \left\lvert\dfrac{\bar{\tau}_{xy}}{\bar{\tau}_{xy}^{y}}\right\rvert^a\right), \\[1em] \left\lvert\dfrac{\bar{\sigma}_{yy}}{\bar{\sigma}_{yy}^{y}} - m_2\dfrac{\bar{\sigma}_{xx}}{\bar{\sigma}_{xx}^{y}}\right\rvert - \left(1 - \left\lvert\dfrac{\bar{\tau}_{xy}}{\bar{\tau}_{xy}^{y}}\right\rvert^b\right) \end{array}\right\} = 0$	for $\begin{cases} \rho < 0.6 & a = 16.52\rho^2 - 23.1\rho + 9.275 \\ 0.6 < \rho < 1 & a = 1.5 \end{cases}$ for $\begin{cases} \rho < 0.6 & b = -11.61\rho^2 + 10.125\rho + 1.05 \\ 0.6 < \rho < 1 & b = 3 \end{cases}$ for $\begin{cases} \rho < 0.6 & m_1 = 1.15e^{6.9\rho} \\ 0.6 < \rho < 1 & m_1 = -205.88\rho^2 + 164.83\rho + 46.97 \end{cases}$ for $\begin{cases} \rho < 0.6 & m_2 = 0.305\rho^{2.35} \\ 0.6 < \rho < 1 & m_2 = 0.3783\rho^{2.811} \end{cases}$

create the STL file of the femur geometry by using the semi-automated segmentation process. The 3D geometry is then created by using SolidWorks® software package, and meshed with tetra-hedron elements in ANSYS (Canonsburg, Pennsylvania, U.S.A). The apparent density ρ for each element of the FE model is then determined from the Hounsfield value (HU) measured from CT data ranging from −1024 HU to 1567 HU. The CT data set represents a regular cubic grid where a HU value is assigned at each point. A linear relation between HU and apparent density is considered. The maximum value of HU corresponds to the densest region of the cortical bone with apparent density of 2.0 g/cm³, and HU value of water and its apparent density equal to zero. Once the apparent density of each CT grid point is obtained, elements of the FE model are superimposed on the CT grid points to evaluate the
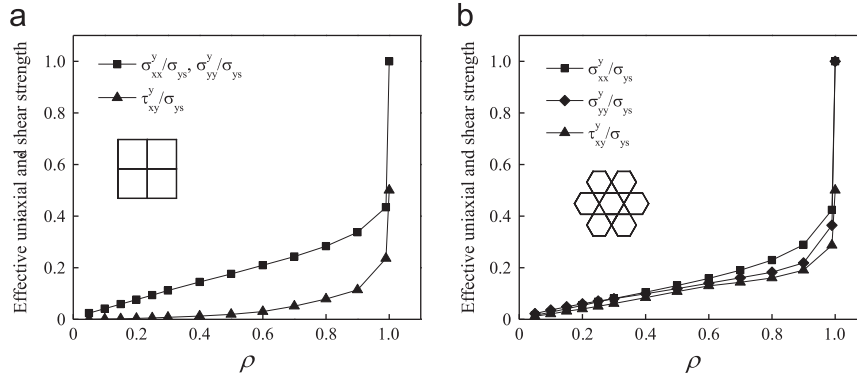
Fig. 4 – Yield strength as a function of relative density for (a) square and (b) Kagome.
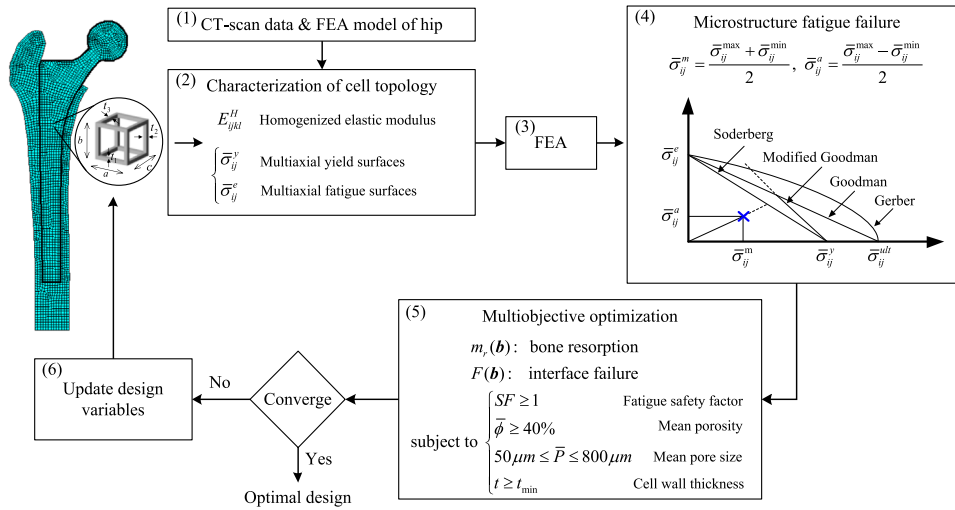
Fig. 5 – Flow chart illustrating the fatigue design methodology of a graded cellular hip implant.

average of relative density for each element using the procedure described in Zannoni et al. (1999). From the apparent density distribution, the effective elastic moduli of bone are obtained through the relation (Austman et al., 2008; Baca et al., 2008; Peng et al., 2006):

$$\begin{cases} E = 1904\rho^{1.64} & \rho < 0.95 \\ E = 2065\rho^{3.09} & 0.95 < \rho \end{cases}, \quad \nu = 0.3 \tag{13}$$

An isotropic material model is considered for the bone, as this simplification does not lead to a noticeable difference from those results obtained by assigning to the bone orthotropic material properties (Baca et al., 2008; Peng et al., 2006).

For the purpose of this exploratory study, the 3D geometry of the femur is simplified to a 2D model, which is assumed to have a side plate of variable thickness (Huiskes, 1990; Weinans et al., 1994). The mid-frontal section of the femur is considered for the 2D model geometry, and the anterior and posterior parts of the femur are represented by the side plate. The 2D model and the side plate have variable thickness such that the second moment of area about the out-of-plane axis of the 2D model does not differ from that of the 3D model (Huiskes et al., 1987; Weinans et al., 1992a, b). The material

properties of the front plate are extracted from the mid-frontal section of the 3D model, and the mechanical properties of the cortical bone are considered for the side plate. This simplification helps reduce the computational cost involved in the optimization process. Nevertheless, many of the essential features of the implant physics can still be captured with a 2D model. For mid-frontal loadings, von Mises and interface stresses distribution can be calculated with an accuracy similar to that of a full 3D model (Weinans et al., 1994). As a result, the remodeling process in the metaphyseal and diaphyseal parts, and the failure at the bone-implant interface, can be approximated with a 2D geometry. The distal end of the femur is fixed to avoid rigid body motion, and three loading cases, 1–3, representing the cyclic load during walking movements are applied to the hip joint and the abductor (Carter et al., 1989; Pérez et al., 2010; Weinans et al., 1992a). With respect to the load cases, magnitude and direction of the hip joint are given here together with the abductor forces in brackets: (1) 2317 N at 24° from vertical (702 N at 28° from vertical), (2) 1158 N at 15° from vertical (351 N at 8° from vertical), (3) 1548 N at 56° from vertical (468 N at 35° from vertical). ANSYS (Canonsburg, Pennsylvania, USA) is used to build, mesh, and solve the 2D model. Assuming in-plane loading conditions, a 2D eight-node element type (Plane 82) is used since it can model curved boundaries with high accuracy.
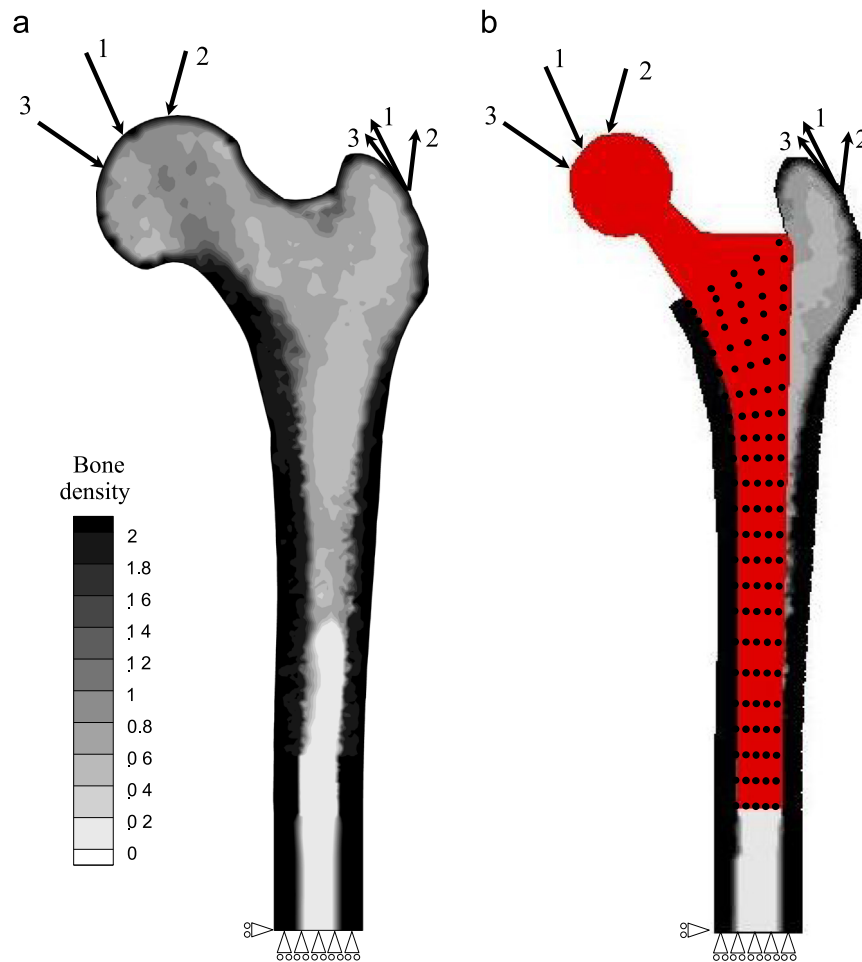
Fig. 6 – (a) 2D Finite element models of the femur and (b) the prosthesis implanted into the femur.

4.2. FEM model of the cellular implant

Fig. 6b illustrates the model of a cementless prosthesis implanted into the femur. The grid depicts the domain of the implant to be designed with a functionally graded lattice material. The variable of the lattice model is the relative density attributed to 115 sampling points, 23 rows along the prosthetic length and 5 columns along the radial direction. The values of relative density are constrained in the range $0.1 \leq \rho \leq 1$ to prevent elastic buckling in the unit cell from occurring prior to yielding (Wang and McDowell, 2004). The relative density distribution throughout the implant is obtained by linear interpolation between the corresponding values at the sampling points. The homogenized stiffness matrix and the yield surfaces of each element are then computed from those values, respectively, illustrated in Fig. 1 and Table 1. The former is employed to assemble the global stiffness matrix for the Finite Element (FE) solver, and the latter is used to construct the Soderberg diagram for fatigue analysis.

Since the implant is designed to have a cellular microstructure with suitable pore size for bone ingrowth, it is assumed that the prosthesis and the surrounding bone are fully bonded (Khanoki and Pasini, 2012; Kowalczyk, 2001). This choice significantly decreases the computational cost required for the stability analysis based on a non-linear frictional contact model (Viceconti et al., 2000). Although bone ingrowth does not exist in a postoperative situation, it can appear later, if local mechanical stability is guaranteed. It is expected, however, that the minimization of interface stress reduces the risk of interface micro-motion and instability (Kowalczyk, 2001).

5. Results

The procedure illustrated in Section 3 is applied for the fatigue design of the implant after having calculated the yield and fatigue strengths of the microstructure, as described in section 2. To solve the multiobjective optimization problem, the non-dominated sorting genetic (NSGA-II) algorithm (Deb et al., 2002) is here used. Once the initial population is evaluated, a set of solutions, called parents, are selected based on their rank and crowding distance. Genetic operators are then applied to the population of parents to create a population of off-springs. Finally, the next population is produced by taking the best solutions from the combined population of parents and off-springs. The optimization continues until the user-defined number of function evaluations reaches 25,000 (Deb et al., 2002). The computational cost required to run the optimization process in a single 2.4 GHz Intel
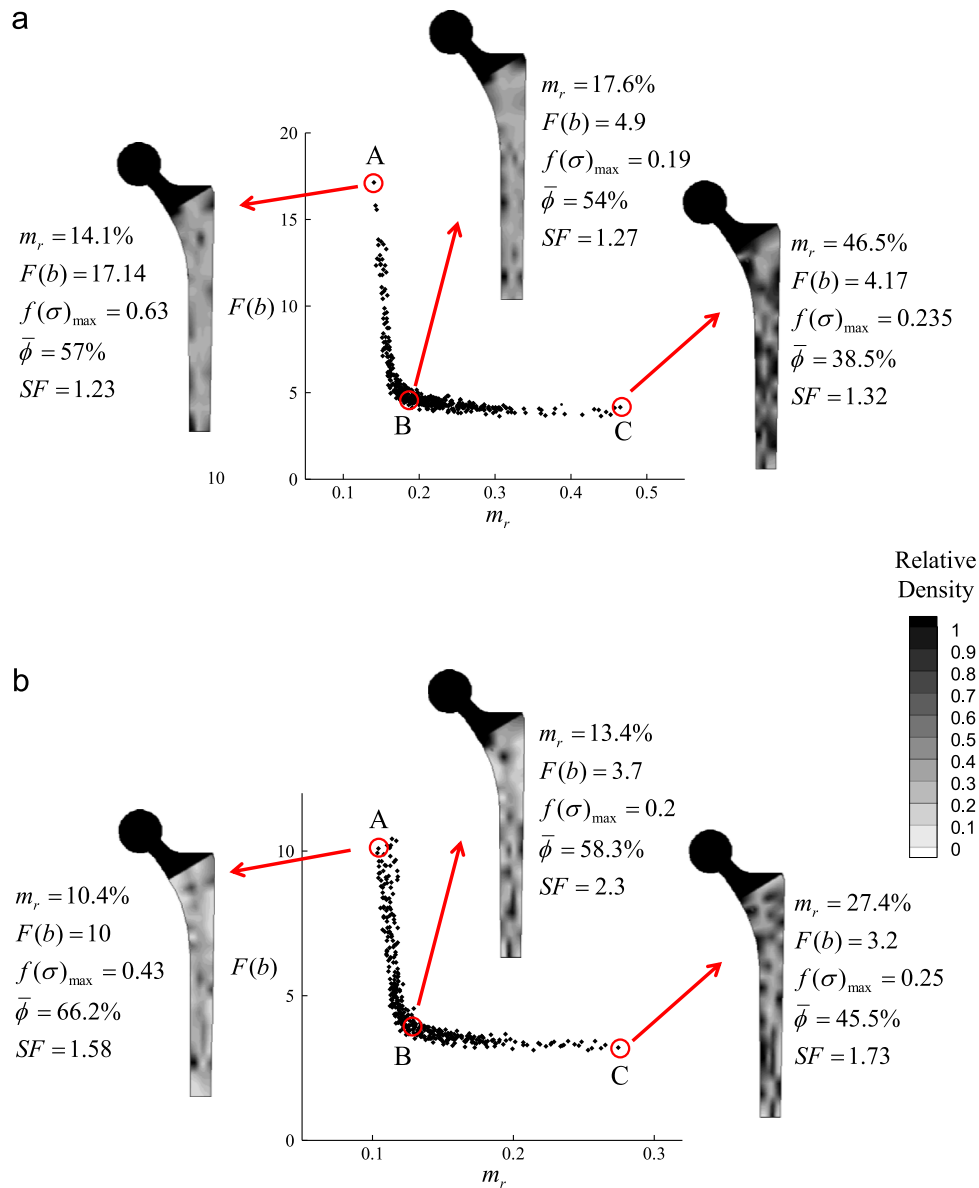
Fig. 7 – Trade-off distributions of relative density for the optimized cellular implant made of (a) square and (b) Kagome lattices.

processor was about 300,000 CPU seconds, 3 days and a half. Parallel computing with a PC cluster will considerably reduce the computational time, since each function evaluation can be performed independently.

Fig. 7(a) and (b) show the optimum relative density distributions for a 2D hip stem designed with square and Kagome cell topologies. The x axis represents the amount of bone resorption for the implanted hip; on the y axis is the interface failure index. Among the optimal solutions, we examine three representative relative density distributions: the extreme points, A and C, of the Pareto frontier, for which one objective function has importance factor 0 and the other 100%, and solution B characterized by weight factors of 50%. For these solutions, the following characteristics are also illustrated in Fig. 7: amount of bone resorption (m_r), interface failure index ($F(b)$), maximum shear interface

failure ($f(\sigma)_{max}$), average porosity of each hip stem ($\bar{\phi}$), and design fatigue safety factor (SF) from the Soderberg diagram.

The advantage of formulating and solving the problem as a multiobjective optimization task is that a set of optimum solutions are available to the user, without requiring to choose in advance any weighting factors for the objective functions. Once the whole set of Pareto solutions has been determined, the surgeon has the freedom to select the desired implant design based on the relative importance of the objective functions. Through a comparison of the results, we observe that an increase in implant porosity from point C to A results in a stiffness decrease of the implant. This increase, on one hand, lowers bone loss, and, on the other, enhances the risk of interface failure. The implant initial stability is the first objective in hip replacement surgery as it governs the long term performance and the

success rate of the implant. Therefore, the implant with maximum stability, solutions C in Fig. 7a and b, might be selected from the Pareto front. By contrasting solutions B and C, we note a significant reduction of bone resorption with only a slight increase of the interface failure index. From solution C to B (Fig. 7a and b), the amount of bone resorption decreases by 62% and 51%, respectively, and the interface failure index increases by 17% and 15%. Solutions B can thus be considered as preferred designs. It should be noted, however, that the selection of the best implant depends also on other factors, such as patient's bone characteristics, the range of activity, age, and the desired level of bone mass preservation after implantation.

As can also be seen compared to the implant with square lattice, the implants designed with Kagome cells have better performance in terms of bone loss and interface shear stress. If solutions B in Fig. 7a and b are compared, we note that the amount of bone loss decreases of about 4.2% and the shear stress concentration factor at the interface reduces by up to about 24.5%.
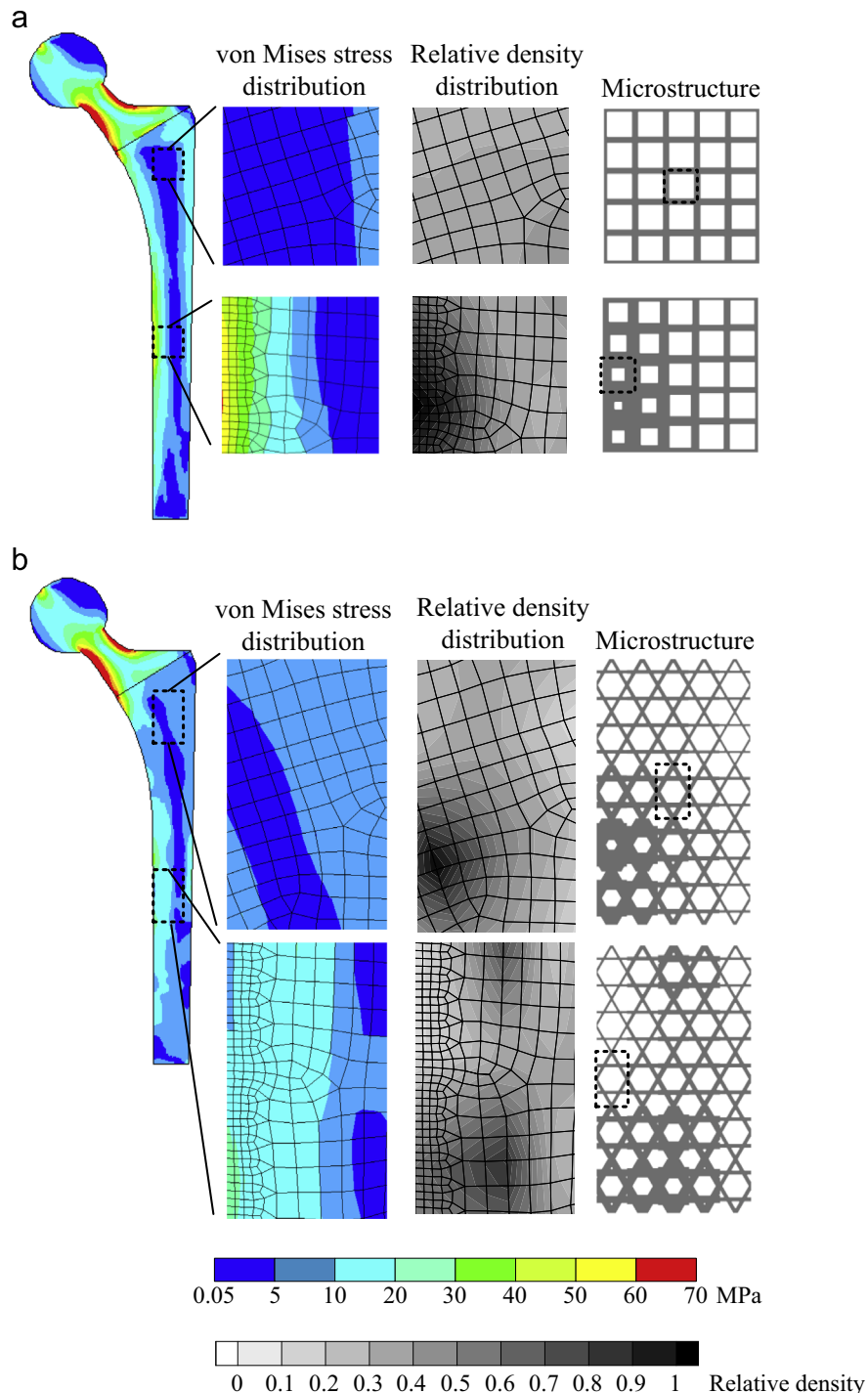

Fig. 8 – Regions used to verify the results of the AH model (left and middle) with respect to a detailed FE analysis of a 5 × 5 lattice microstructure (right).

While both implants have been designed for infinite fatigue life, the fatigue safety factor has improved approximately 81% for the implant designed by the graded Kagome cell topology. The reason for this is that Kagome is a stretching dominated cell with higher mechanical strength compared to the square cell for a given relative density. This provides a wider range of relative density for the optimization search to choose the design variable from, and control the stress distribution at the interface. Moreover, lower values of relative density can be selected to increase the implant flexibility and reduce bone resorption. We remark here that beside mechanical strength, other physical parameters, such as pore shape, interconnectivity, permeability and diffusivity of the unit cell, should be taken into account for the selection of a proper lattice cell for bone tissue scaffolding (Hollister, 2005; Hollister et al., 2008; Kang et al., 2010; Reilly and Engler, 2010; Van Bael et al., 2012). Further research is required in the near future to address these aspects.

6. Verification of the numerical results

During the optimization procedure, AH is applied for the multi-scale analysis of the cellular implants. Although this method is quite effective in computing the stress and strain distribution at each scale, the results needs to be verified especially at regions where the underlying assumption, Y-periodicity of field quantities, is not satisfied. This can include regions with locally varying structure, areas with a high gradient of field quantities, or zones in the vicinity of borders (Dumontet, 1986; Ghosh et al., 2001; Lefik and Schrefler, 1996; Raghavan and Ghosh, 2004; Takano et al., 2003; Yuan and Pagano, 2003). The multilevel computational method can be used for the analysis of these critical regions (Ghosh et al., 2001; Raghavan and Ghosh, 2004). This method decomposes the computational domain into two levels of hierarchy: (a) the detailed cellular microstructure and (b) the homogenized medium. The region of interest, composed of a cellular microstructure, is modeled by a fully detailed FE analysis, and the results are compared with those obtained from the homogenization method to verify the periodicity assumption of AH. The following criterion can be defined to measure the departure from the periodicity conditions:

$$\frac{F(\sigma_{ij},\varepsilon_{ij})^{FEA}-F(\sigma_{ij},\varepsilon_{ij})^{RVE}}{F(\sigma_{ij},\varepsilon_{ij})^{RVE}}\geq C \tag{14}$$

where the function F is a function of $(\sigma_{ij},\varepsilon_{ij})$ and can be defined, for example, as the average of the microscopic stress over the RVE. The superscript FEA refers to the evaluation of the function F via a detailed finite element analysis of a given microstructure. The macroscopic displacement solution, obtained from the homogenized model, is imposed on the unit cell boundary of the detailed FE model, and the stress and strain distribution within the microstructure is obtained. The superscript RVE, on the other hand, corresponds to the computation of F for each RVE through the imposition to the unit cell of a macroscopic strain with periodic boundary conditions. C is a user defined adaptation tolerance; $C=0.1$ can be considered as an appropriate transition value to map the homogenized model to the detailed analysis of the local microstructure (Raghavan and Ghosh, 2004). Here as functions, (a) the average and (b) the maximum value of von Mises stress over the unit cell, are considered, respectively, to verify the periodicity assumption of field quantities at the macroscale, and to assess the estimation of material yield in the lattice.

We investigate two regions to verify the results of AH: one at the proximal part, where the Y-periodic assumption of field quantities is expected, and the other at the vicinity of the implant boundary, where this assumption does not hold. Fig. 8 illustrates the macroscopic von Mises stress distribution throughout the square and Kagome lattice implants associated with the loading condition number 1 applied to the hip joint. The mesh of the macroscopic elements at the vicinity of the implant border has been refined to capture the interface stresses with a higher resolution. The stress and relative density distribution, shown in Fig. 8, corresponds to the solutions B in Fig. 7. We can observe almost a uniform stress distribution in the proximal region of the implants; however, there is higher stress gradient at the vicinity of the implant boundary especially for the square lattice implant, which might affect the periodicity assumption of AH. To perform the detailed FEA and verify the results of AH, the microstructures need to be constructed at the specified regions. For the square cell, a 2 mm × 2 mm size is selected to satisfy the manufacturing constraint ($t_{min}\geq 0.1$ mm for $\rho\geq 0.1$) and to uniformly tessellate the regions with a 5 × 5 cells block. For the Kagome topology, the RVE has a rectangular shape with the same cell size as the square in the x direction. To produce
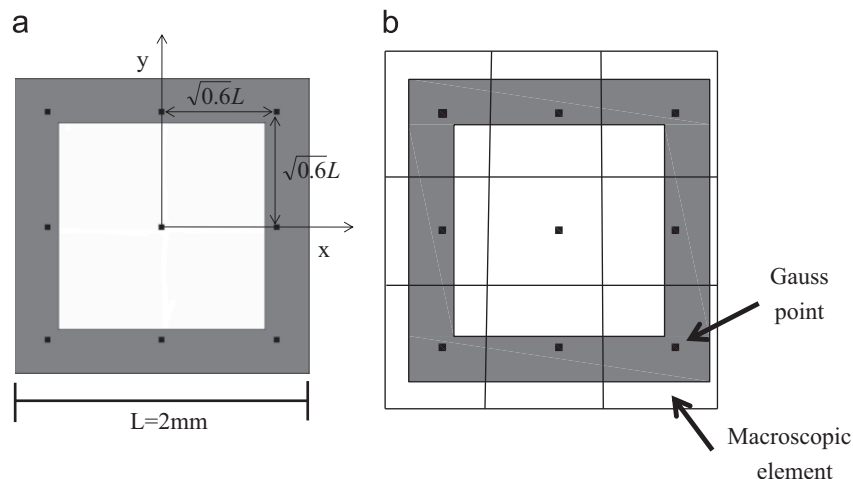

Fig. 9 – (a) 3 × 3 Gauss points in the RVE; (b) superposition of the RVE on the macroscopic mesh of the homogenized model.

the cell geometry from the relative density distribution, 3×3 Gauss points are assigned to each cell, as shown in Fig. 9. Using a Gaussian quadrature integration (Zienkiewicz and Taylor, 2005), the average relative density of the RVE is obtained as:

$$\bar{\rho} = \sum_{i=1}^{9} \sum_{j=1}^{9} W_{ij}\rho_{ij} \qquad (15)$$

where ρ_{ij} and W_{ij} are the relative density and weight factors at each Gauss point, respectively. The relative density at each Gauss point is obtained with respect to its local coordinates within the macroscopic element of the homogenized model (Fig. 9). Once the average relative density is obtained, the cell geometry can be constructed for both the square and Kagome lattices, as depicted in Fig. 8. The displacement of the macroscopic solution is then imposed on the boundary of the cells block (Raghavan and Ghosh, 2004), so as to calculate the stress distribution of the microstructure. The average and the maximum von Mises stress for the unit cells is then computed and used in Eq. (14) to verify the periodicity assumption and the results of AH.

To recover the stress distribution throughout the microstructure via AH, the average macroscopic strain is needed over the RVE. Fig. 10 illustrates the macroscopic strains distribution, $\bar{\varepsilon}_{xx}, \bar{\varepsilon}_{yy}, \bar{\tau}_{xy}$, over the regions proximal and closed to the boundary of the square and Kagome lattice implants. As can be seen, there is a uniform variation of macroscopic strains in the proximal region, while there is high strain gradient close to the boundary which might affect the AH periodicity assumption. Therefore, the results obtained by the homogenization method needs to be verified. Using the procedure described above, the average macroscopic strain for each unit cell is computed; the strain tensor is used in Eq. (2) to obtain the microscopic strain distribution throughout the microstructure, from which the microscopic stresses are calculated via the constitutive equation of the base material. For the block at the proximal region, the microscopic stress distribution of the unit cell located at the center of the block is compared with those obtained from a detailed
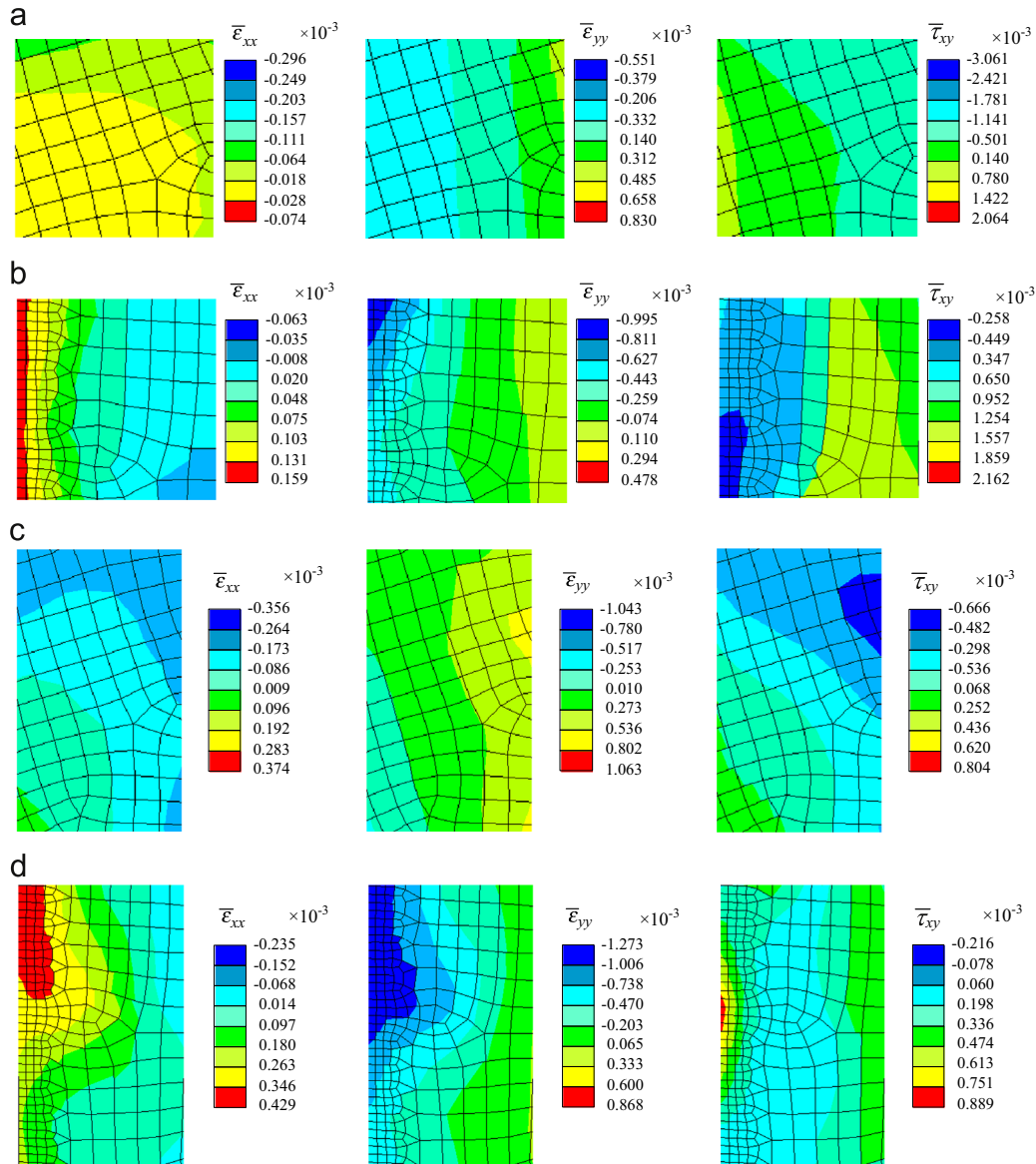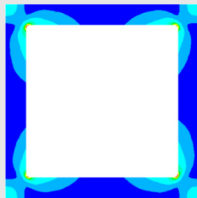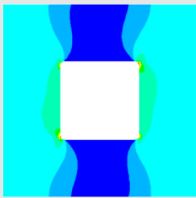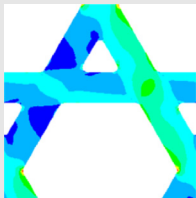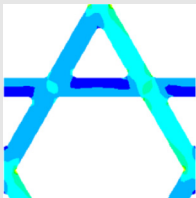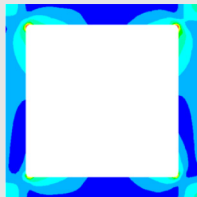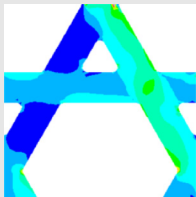

Fig. 10 – Macroscopic strain distribution (solution B in Fig. 7a and Fig. 7b) as a result of load case 1 at (a) the proximal part and (b) the border of the square lattice implant, and (c) the proximal part and (d) the border of the Kagome lattice implant.

Table 2 – Comparison of microscopic stress distribution obtained by detailed FEA and AH for the unit cells located at the proximal region and closed to the implant border.

	Proximal cell	Boundary cell	Proximal cell	Boundary cell
AH				
FEA				
Error $(\bar{\sigma}_{vM})^{a}$	0.98%	1.8%	1.2%	3.8%
Error $(max\{\sigma_{vM}\})^{b}$	7.1%	8.7%	8.2%	18.6%

[a] The error corresponds to the average of von Mises stress over the unit cell.
[b] The error corresponds to the maximum von Mises stress over the unit cell.

FEA. For the block at the implant border, the stress distribution within the cell in the middle of the first column of Fig. 8 is considered. Based on the results of several analyses, we have observed that a change of the block position has a negligible effect on the unit cell stress distribution if the location of the selected unit cell is prescribed within the implant.

The von Mises stress distribution of the unit cells, obtained by AH and by detailed FE analysis, are given in Table 2. The average and the maximum value of von Mises stress over the unit cells obtained by AH are also compared with the detailed FE analysis, and the relative errors, defined by Eq. (14), are illustrated in Table 2. For the square unit cell located in the proximal region, the average and the maximum value of von Mises stress can be estimated with an error of 0.98% and 7.1%, respectively. However, for the unit cells close to the boundary, a higher relative error for the microscopic stresses is observed as the Y-periodic assumption is not satisfied. For the Kagome lattice located in the proximal region, the relative error for the average and the maximum von Mises stress is 1.2% and 8.2%, respectively, percentages that increase to 3.8 and 18.6 when the Kagome unit cell is located at the implant boundary. Considering $C=0.1$ as the criterion for creating the transition from the homogenized model to the fully detail analysis, it can be seen that the periodicity assumption can capture the average of the macroscopic stress distribution throughout the implant with an error below 0.1. The average macroscopic stress in Table 1 can be used to assess the material yield at the microscopic level of the lattice struts. For unit cells located at the

implant boundary, where non-periodic local heterogeneity and non-uniform macroscopic field exist, the finite element mesh superposition method integrated with AH is better suited to capture the microscopic stress distribution with higher accuracy (Takano et al., 2010, 2000, 2003; Takano and Okuno, 2004). This would significantly reduce the computational cost of the numerical simulations, since a fully detailed FEA of the implant might be unfeasible. The computational cost required to perform a single simulation of a fully detailed FE model of a cellular implant on a 2.4 GHz Intel processor is about 1500 CPU seconds. Considering 25,000 function evaluations for the optimization procedure, the simulation time required for the fully detailed FE model would be 3.75×10^{7} s which is about 100 times higher than the simulation time needed for the analysis of a homogenized model.

7. Discussions

In this section, we examine the results within the context of a performance comparison of other implants currently available in the market as well as on the manufacturability aspects. As a benchmark for the comparative study, a fully dense titanium implant is chosen. Its bone resorption and the distribution of local shear interface failure are determined, and then compared with those of the cellular implants represented by solutions B in Fig. 7 for both the square and Kagome lattice.
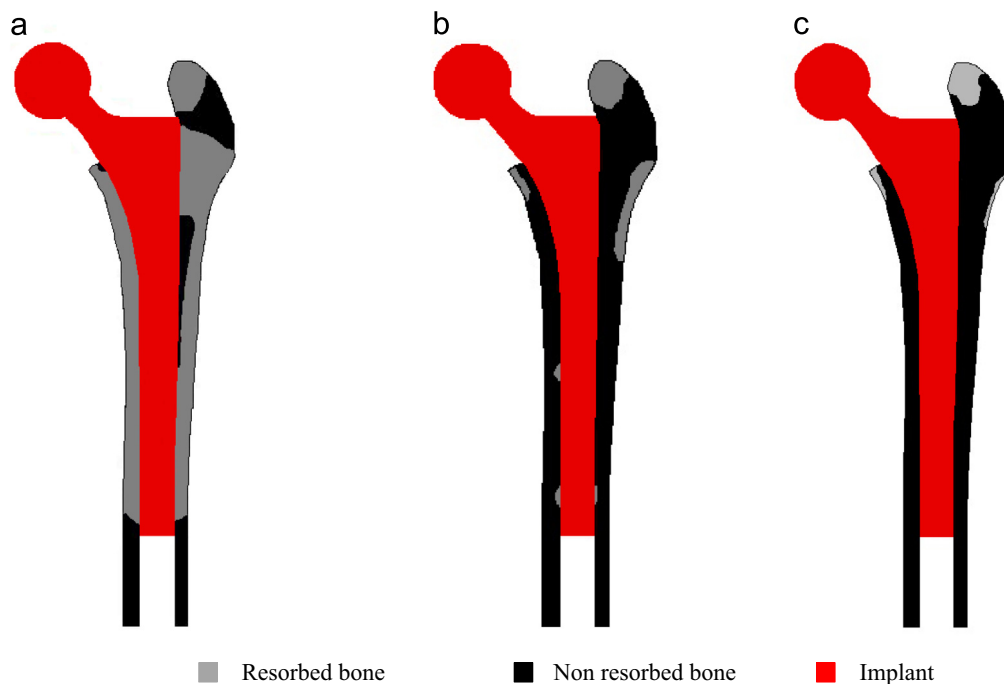
Fig. 11 – Distribution of bone resorption around (a) fully dense titanium implant, (b) graded cellular implant with square topology (solution B in Fig. 7a), (c) graded cellular implant with Kagome topology (solution B in Fig. 7b).

As expected, Fig. 11a shows that for a fully dense implant, bone mass loss is about 71.4%. This initial postoperative configuration of bone loss is in good agreement with that in literature (Huiskes et al., 1992; Weinans et al., 1992a). A high amount of bone resorption is found throughout the medial and lateral part of the femur around the fully dense stem. Compared to the fully dense implant, the amount of initial postoperative bone loss of the square and Kagome lattice implants decreases, respectively, by 53.8% and 58%. This shows that the design of a flexible implant through a graded cellular material has the beneficial effect of improving the load-sharing capacity of the implant with the surrounding bone, thereby reducing bone resorption.

Fig. 12 shows the distribution of the local shear interface failure, $f(\sigma)$, around the fully dense titanium, square and Kagome lattice implants. At each point, the maximum value of interface failure caused by any of three loading cases is shown. Since the function $f(\sigma)$ is the interface shear stress normalized with respect to the local shear strength of the bone, high probability of interface failure is expected for $f(\sigma) \geq 1$, whereas for $f(\sigma) < 1$ the risk of interface failure is low. For the fully dense titanium implant, we observe that the maximum value of shear interface failure occurs at the distal end with magnitude of 0.96. This means that the shear stress is almost equal to the shear strength of the host bone, which may cause interface micromotion and prevent bone ingrowth. For the square and Kagome lattice implants, the maximum shear interface failure reduces significantly of about 79% to 0.19 and 0.2, respectively. An optimized graded distribution of the cellular microarchitecture can reduce the stress distribution at the implant interface. For the numerical verification, the interface shear stress of fully dense titanium implant is also compared with those obtained in literature (Kuiper and Huiskes, 1992, 1996). We have that the

interface shear stress varies from 3.8 MPa at the proximal region to the maximum value of 42 MPa at the distal end, which is in good agreement with the stress regime available in (Kuiper and Huiskes, 1992, 1996).

The fatigue analysis of the fully dense titanium implant shows that its safety factor is 4.95. Although this value is about two times higher than the corresponding value of the Kagome lattice implant, a safety factor of 2.3 for Kagome lattice implant can be still considered as a reasonably safe margin for the design against fatigue fracture. To improve the implant fatigue strength, either a lattice with smooth cell geometry could be considered (Abad et al., 2012), or the implant core can be designed as fully dense.

To assess the manufacturability of the implant microarchitecture, 2D proof-of-concepts implants were fabricated via EBM. Ti6Al4V powder supplied by ARCAM (2013) with powder particle size between 45 μm and 100 μm was used for fabrication. The relative density distribution of solution C in Fig. 7a was selected and mapped into a square lattice implant with the following cell size: 1 mm, 2 mm, and 3 mm. A uniform cell tessellation was assumed to draw the geometric model. 3×3 Gauss points were assigned to each cell, and the average of relative density was computed through Eq. (15). The geometry of each lattice cell was then calculated from the average relative density and the size of the unit cell. STL files of the cellular implants were created and finally processed by EBM.

Fig. 13 shows the implants with their representative microstructure. An optical microscope equipped with a digital camera was used to measure morphological parameters of the cell, such as cell wall thickness and pore size. No sign of fracture or incomplete cell walls was inspected, an observation that shows good metallurgic bond between cell walls and structural integrity of the lattice. Fig. 14 provides the comparison of the average cell
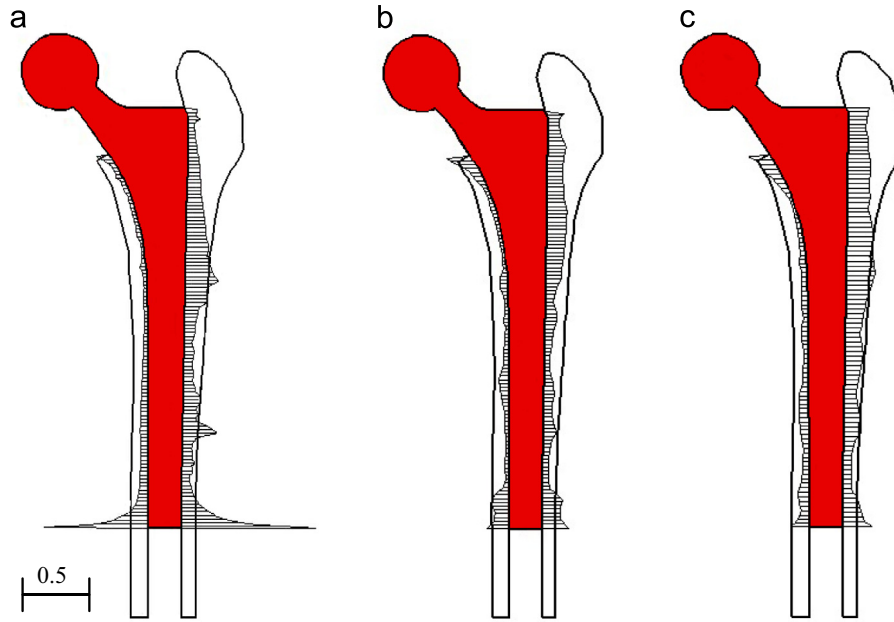
Fig. 12 – Distribution of local shear interface failure $f(\sigma)$ around (a) fully dense titanium implant, (b) graded cellular implant with square topology (solution B in Fig. 7a), (c) graded cellular implant with Kagome topology (solution B in Fig. 7b).
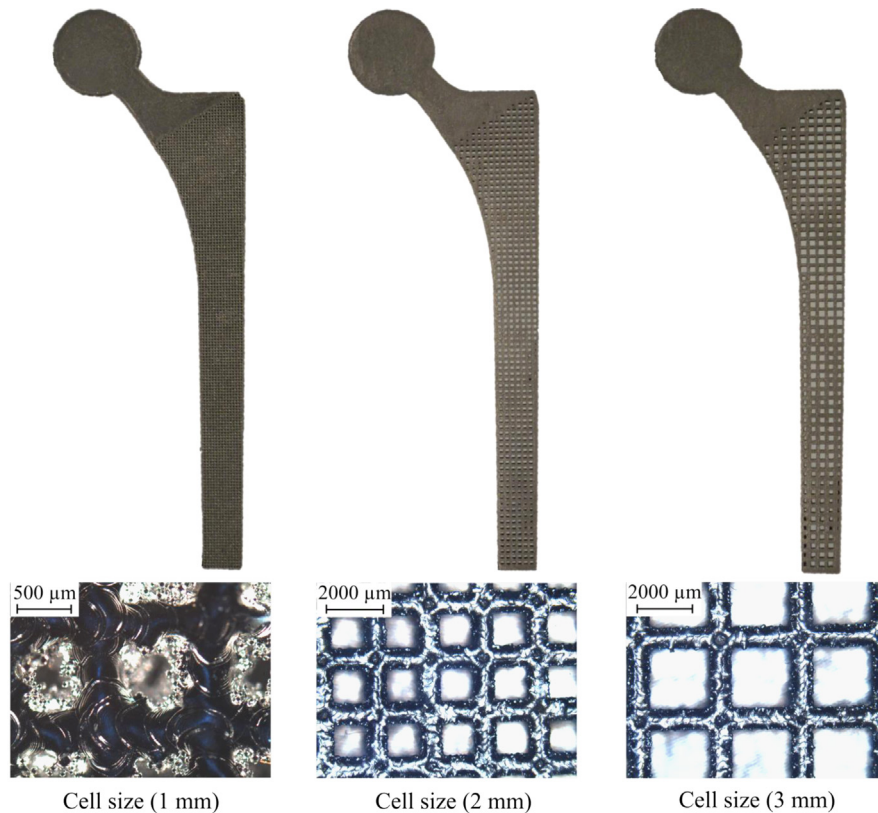

Fig. 13 – Fabricated Ti6Al4V graded cellular implants with their corresponding microstructure.

wall thickness and pore size between the nominal values and the fabricated parameters for each prototype.

For the implant with unit cell size of 1mm, the average wall thickness and pore size exhibit a high relative error. The average wall

thickness of the fabricated implant is 33.5% higher than the nominal value, while its average pore size is 53.6% lower than the nominal one. As can be seen in Fig. 13, the pores are partially filled with non-fully melted powder particles, a side-effect that increases the wall
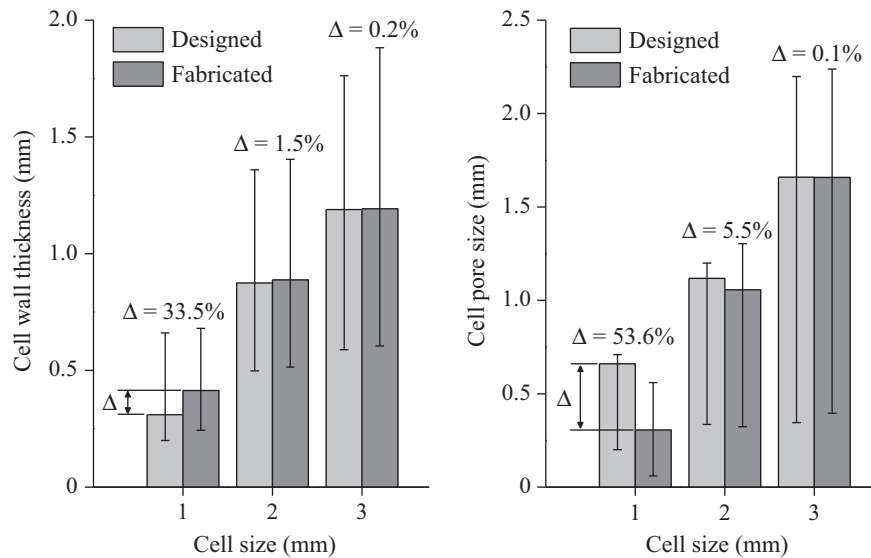
Fig. 14 – Cell wall thickness and pore size of cellular implants fabricated with alternative cell size are compared to the nominal design parameters. Δ represents the difference between the average as-fabricated and the nominal values.

thickness and decreases the effective pore size. Although the pores size range between 60 μm and 560 μm is still an optimum range for bone ingrowth, the average pore size has decreased of 46%, from the nominal value of 660 μm to the real size of 306 μm.

On the other hand, for cell size of 2 mm and 3 mm, the morphological parameters are in a good agreement with the design values. The difference between the average pore size decreases from 5.5% for 2 mm unit cell size to a negligible value of 0.1% for 3 mm cell size. While a cell size increase provides more control on the results, it may lead to a pore size greater than the suitable size for bone ingrowth. For the prototype with unit cell size of 2 mm, the pore size varies between 323 μm and 1305 μm with an average of 1040 μm; this value is slightly higher than the optimum size for bone ingrowth. For the implant with unit cell size of 3 mm, the pore size range is between 395 μm and 2240 μm with an average of 1660 μm, which is significantly higher than the optimum size prescribed for bone ingrowth. To provide a suitable environment for bone ingrowth, a periphery layer with either a smaller unit cell size or a conventional porous coating is suggested to be integrated on the implant surface.

Exploratory in nature, this study holds some limitations, which are here discussed. For the numerical simulation, the material has been assumed free of defects with mechanical properties comparable to those of the bulk material. The effect of unevenness of samples surface leading to surface curvatures and corrugation could be also accounted for. These defects result in local non-periodic heterogeneities and stress concentrations which affect the stiffness and strength of the lattice. A multiscale finite element analysis (Takano et al., 2010, 2003; Takano and Okuno, 2004) combining enhanced mesh superposition method with AH theory could be implemented. In addition, further work is required to examine the sensitivity of the results to variations of bulk material properties. Another aspect is the simplification of the 3D model of the implanted femur to a 2D model. To extend the proposed procedure to three dimensions, the 3D geometry of the implanted femur should be created. Then the topology of the three-dimensional lattice at the periphery of the implant should be selected to respect desired values of porosity and cell

interconnectivity (Cheah et al., 2003a, b) to meet bone vascularization requirements. Finally, more detailed models on bone resorption (Boyle and Kim, 2011a, b; Weinans et al., 1992a, b) and implant stability (Abdul-Kadir et al., 2008; Viceconti et al., 2006, 2001, 2000) could be used to assess both the short and long term performance of the implant.

8.   Conclusions

A hip-joint implant with a graded lattice material can improve the load sharing capacity of the implant with the surrounding bone tissues as well as decrease the amount of bone resorption. In this study, the lattice microarchitecture of a 2D proof-of-concept implant has been designed against fatigue fracture to support cyclic loads in the hip joint. Asymptotic homogenization has been used for the multiscale analysis of the structure to obtain the stress distribution at the macro and micro scale, while the Soderberg fatigue criterion has been integrated in the procedure to design the implant for infinite fatigue life. The numerical results obtained have been verified via a detailed FE analysis. Square and Kagome lattices have been used in a multiobjective optimization procedure to simultaneously minimize bone resorption and interface failure. It has been found that for the square and Kagome lattice implants the amount of bone loss is respectively 54% and 58% lower than that of a fully dense titanium implant. The maximum shear interface failure at the distal end of the implants decreases as well of about 79%. Finally, a set of 2D proof-of-concepts have been fabricated with EBM to demonstrate the manufacturability of the lattice implants.

REFERENCES

Abad, E.M.K., Khanoki, S.A., Pasini, D., 2012. Fatigue design of lattice materials via computational mechanics: application to lattices

with smooth transitions in cell geometry. International Journal of Fatigue.

Abdul-Kadir, M.R., Hansen, U., Klabunde, R., Lucas, D., Amis, A., 2008. Finite element modelling of primary hip stem stability: the effect of interference fit. Journal of Biomechanics 41, 587–594.

ARCAM, 2013. Ti6Al4V Titanium Alloy.

Austman, R.L., Milner, J.S., Holdsworth, D.W., Dunning, C.E., 2008. The effect of the density–modulus relationship selected to apply material properties in a finite element model of long bone. Journal of Biomechanics 41, 3171–3176.

Baca, V., Horak, Z., Mikulenka, P., Dzupa, V., 2008. Comparison of an inhomogeneous orthotropic and isotropic material models used for FE analyses. Medical Engineering & Physics 30, 924–930.

Baleani, M., Cristofolini, L., Viceconti, M., 1999. Endurance testing of hip prostheses: a comparison between the load fixed in ISO 7206 standard and the physiological loads. Clinical Biomechanics 14, 339–345.

Behrens, B., Wirth, C., Windhagen, H., Nolte, I., Meyer-Lindenberg, A., Bouguecha, A., 2008. Numerical investigations of stress shielding in total hip prostheses. Proceedings of the Institution of Mechanical Engineers Part H: Journal of Engineering in Medicine 222, 593–600.

Bendsøe, M.P., Kikuchi, N., 1988. Generating optimal topologies in structural design using a homogenization method. Computer Methods in Applied Mechanics and Engineering 71, 197–224.

Bendsøe, M.P., Sigmund, O., 2003. Topology Optimization: Theory, Methods, and Applications. Springer Verlag, Berlin, Heidelberd, New York.

Bobyn, J.D., Poggie, R., Krygier, J., Lewallen, D., Hanssen, A., Lewis, R., Unger, A., O'keefe, T., Christie, M., Nasser, S., 2004. Clinical validation of a structural porous tantalum biomaterial for adult reconstruction. The Journal of Bone and Joint Surgery 86, 123–129.

Boyle, C., Kim, I.Y., 2011a. Comparison of different hip prosthesis shapes considering micro-level bone remodeling and stress-shielding criteria using three-dimensional design space topology optimization. Journal of Biomechanics 44, 1722–1728.

Boyle, C., Kim, I.Y., 2011b. Three-dimensional micro-level computational study of Wolff's law via trabecular bone remodeling in the human proximal femur using design space topology optimization. Journal of Biomechanics 44, 935–942.

Bragdon, C., Jasty, M., Greene, M., Rubash, H., Harris, W., 2004. Biologic fixation of total hip implants: insights gained from a series of canine studies. The Journal of Bone and Joint Surgery 86, 105–117.

Carter, D., Orr, T., Fyhrie, D., 1989. Relationships between loading history and femoral cancellous bone architecture. Journal of Biomechanics 22, 231–244.

Cheah, C., Chua, C., Leong, K., Chua, S., 2003a. Development of a tissue engineering scaffold structure library for rapid prototyping. Part 1: Investigation and classification. The International Journal of Advanced Manufacturing Technology 21, 291–301.

Cheah, C., Chua, C., Leong, K., Chua, S., 2003b. Development of a tissue engineering scaffold structure library for rapid prototyping. Part 2: Parametric library and assembly program. The International Journal of Advanced Manufacturing Technology 21, 302–312.

Coelho, P., Fernandes, P., Guedes, J., Rodrigues, H., 2008. A hierarchical model for concurrent material and topology optimisation of three-dimensional structures. Structural and Multidisciplinary Optimization 35, 107–115.

Coelho, P.G., Cardoso, J.B., Fernandes, P.R., Rodrigues, H.C., 2011. Parallel computing techniques applied to the simultaneous design of structure and material. Advances in Engineering Software 42, 219–227.

Cote, F., Deshpande, V., Fleck, N., Evans, A., 2006. The compressive and shear responses of corrugated and diamond lattice materials. International Journal of Solids and Structures 43, 6220–6242.

Côté, F., Deshpande, V.S., Fleck, N.A., 2007a. Shear fatigue strength of a prismatic diamond sandwich core. Scripta Materialia 56, 585–588.

Côté, F., Fleck, N.A., Deshpande, V.S., 2007b. Fatigue performance of sandwich beams with a pyramidal core. International Journal of Fatigue 29, 1402–1412.

Deb, K., Pratap, A., Agarwal, S., Meyarivan, T., 2002. A fast and elitist multiobjective genetic algorithm: NSGA-II. IEEE Transactions on Evolutionary Computation 6, 182–197.

Díaaz, A., Kikuchi, N., 1992. Solutions to shape and topology eigenvalue optimization problems using a homogenization method. International Journal for Numerical Methods in Engineering 35, 1487–1502.

Dumontet, H., 1986. Study of a boundary layer problem in elastic composite materials. RAIRO Modél. Math. Anal. Numér 20, 265–286.

Geetha, M., Singh, A.K., Asokamani, R., Gogia, A.K., 2009. Ti based biomaterials, the ultimate choice for orthopaedic implants—a review. Progress in Materials Science 54, 397–425.

Ghosh, S., Lee, K., Raghavan, P., 2001. A multi-level computational model for multi-scale damage analysis in composite and porous materials. International Journal of Solids and Structures 38, 2335–2385.

Gibson, L.J., 2005. Biomechanics of cellular solids. Journal of Biomechanics 38, 377–399.

Glassman, A., Bobyn, J., Tanzer, M., 2006. New femoral designs do they influence stress shielding?. Clinical Orthopaedics and Related Research 453, 64–74.

Gonçalves Coelho, P., Rui Fernandes, P., Carriço Rodrigues, H., 2011. Multiscale modeling of bone tissue with surface and permeability control. Journal of Biomechanics 44, 321–329.

Guedes, J., Kikuchi, N., 1990. Preprocessing and postprocessing for materials based on the homogenization method with adaptive finite element methods. Computer Methods in Applied Mechanics and Engineering 83, 143–198.

Harrysson, O.L.A., Cansizoglu, O., Marcellin-Little, D.J., Cormier, D.R., West, Ii, H.A., 2008. Direct metal fabrication of titanium implants with tailored materials and mechanical properties using electron beam melting technology. Materials Science and Engineering C 28, 366–373.

Hassani, B., 1996. A direct method to derive the boundary conditions of the homogenization equation for symmetric cells. Communications in numerical methods in engineering 12, 185–196.

Hassani, B., Hinton, E., 1998. A review of homogenization and topology optimization I I I–topology optimization using optimality criteria. Computers & Structures 69, 739–756.

Hedia, H., Barton, D., Fisher, J., Elmidany, T., 1996. A method for shape optimization of a hip prosthesis to maximize the fatigue life of the cement. Medical Engineering & Physics 18, 647–654.

Hollister, S., Kikuchi, N., 1992. A comparison of homogenization and standard mechanics analyses for periodic porous composites. Computational Mechanics 10, 73–95.

Hollister, S.J., 2005. Porous scaffold design for tissue engineering. Nature materials 4, 518–524.

Hollister, S.J., Lin, C.Y., Kang, H., Adachi, T., 2008. Computational design and simulation of tissue engineering scaffolds. Virtual Prototyping & Bio Manufacturing in Medical Applications, 113–127.

Huang, J.-S., Liu, S.-Y., 2001a. Fatigue of honeycombs under in-plane multiaxial loads. Materials Science and Engineering A 308, 45–52.

Huang, J.-S., Liu, S.-Y., 2001b. Fatigue of isotropic open-cell foams under multiaxial loads. International Journal of Fatigue 23, 233–240.

Huang, J.S., Lin, J.Y., 1996. Fatigue of cellular materials. Acta Materialia 44, 289–296.

Huiskes, R., 1990. The various stress patterns of press-fit, ingrown, and cemented femoral stems. Clinical Orthopaedics and Related Research 261, 27.

R. Huiskes, H. Weinans, H. J. Grootenboer, M. Dalstra, B. Fudala, and T. J. Slooff, "Adaptive bone-remodeling theory applied to prosthetic-

design analysis," Journal of Biomechanics, vol. 20, pp. 1135-1150, 1987.

Huiskes, R., Weinans, H., Rietbergen, B., 1992. The relationship between stress shielding and bone resorption around total hip stems and the effects of flexible materials. Clinical Orthopaedics and Related Research 274, 124–134.

Kalamkarov, A.L., Andrianov, I.V., Danishevs'kyy, V.V., 2009. Asymptotic homogenization of composite materials and structures. Applied Mechanics Reviews 62, 030802.

Kang, H., Lin, C.Y., Hollister, S.J., 2010. Topology optimization of three dimensional tissue engineering scaffold architectures for prescribed bulk modulus and diffusivity. Structural and Multidisciplinary Optimization 42, 633–644.

Kanouté, P., Boso, D., Chaboche, J., Schrefler, B., 2009. Multiscale methods for composites: a review. Archives of Computational Methods in Engineering 16, 31–75.

Kayabasi, O., Ekici, B., 2007. The effects of static, dynamic and fatigue behavior on three-dimensional shape optimization of hip prosthesis by finite element method. Materials & Design 28, 2269–2277.

Khanoki, S.A., Pasini, D., 2012. Multiscale design and multiobjective optimization of orthopedic hip implants with functionally graded cellular material. Journal of Biomechanical Engineering 134, 031004.

Kowalczyk, P., 2001. Design optimization of cementless femoral hip prostheses using finite element analysis. Journal of Biomechanical Engineering 123, 396–402.

Kuiper, J., Huiskes, R., 1992. Numerical optimization of hip-prosthetic stem material. Recent Advances in Computer Methods in Biomechanics & Biomedical Engineering. J. Mddleton, GN Pande, and KR Williams, 76–84.

Kuiper, J., Huiskes, R., 1996. Friction and stem stiffness affect dynamic interface motion in total hip replacement. Journal of Orthopaedic Research 14, 36–43.

Lefik, M., Schrefler, B., 1996. F E modelling of a boundary layer corrector for composites using the homogenization theory. Engineering Computations 13, 31–42.

Li, C, Granger, C., Schutte, H.D., Biggers, S.B., Kennedy, J.M., Latour, R. A., 2002. Progressive failure analysis of laminated composite femoral prostheses for total hip arthroplasty. Biomaterials 23, 4249–4262.

Li, S.J., Murr, L.E., Cheng, X.Y., Zhang, Z.B., Hao, Y.L., Yang, R., Medina, F., Wicker, R.B., 2012. Compression fatigue behavior of Ti-6Al-4V mesh arrays fabricated by electron beam melting. Acta Materialia 60, 793–802.

Li, X., Wang, C., Zhang, W., Li, Y., 2010. Fabrication and compressive properties of Ti6Al4V implant with honeycomb-like structure for biomedical applications. Rapid Prototyping Journal 16, 44–49.

Liu, P.S., Du, H.Y., 2011. Modeling failure modes of isotropic three-dimensional reticulated porous metal foams under several typical loads. Materials & Design 32, 4786–4793.

Marin, E., Fusi, S., Pressacco, M., Paussa, L., Fedrizzi, L., 2010. Characterization of cellular solids in Ti6Al4V for orthopaedic implant applications: trabecular titanium. Journal of the Mechanical Behavior of Biomedical Materials 3, 373–381.

Murr, L., Gaytan, S., Medina, F., Lopez, H., Martinez, E., Machado, B., Hernandez, D., Martinez, L., Lopez, M., Wicker, R., 2010. Next-generation biomedical implants using additive manufacturing of complex, cellular and functional mesh arrays. Philosophical Transactions of the Royal Society of London, Series A: Mathematical, Physical and Engineering Sciences 368, 1999–2032.

Murr, L.E., Gaytan, S.M., Martinez, E., Medina, F., Wicker, R.B., 2012. Next generation orthopaedic implants by additive manufacturing using electron beam melting. International Journal of Biomaterials 2012.

Murr, L.E., Quinones, S.A., Gaytan, S.M., Lopez, M.I., Rodela, A., Martinez, E.Y., Hernandez, D.H., Martinez, E., Medina, F., Wicker, R. B., 2009. Microstructure and mechanical behavior of Ti-6Al-4V

produced by rapid-layer manufacturing, for biomedical applications. Journal of the Mechanical Behavior of Biomedical Materials 2, 20–32.

Nganbe, M., Khan, U., Louati, H., Speirs, A., Beaulé, P.E., 2011. In vitro assessment of strength, fatigue durability, and disassembly of Ti4Al4V and CoCrMo necks in modular total hip replacements. Journal of Biomedical Materials Research Part B: Applied Biomaterials 97B, 132–138.

Nicholas, T., Zuiker, J., 1989. On the use of the Goodman diagram for high cycle fatigue design. International Journal of Fracture 80, 219–235.

Olurin, O., McCullough, K., Fleck, N., Ashby, M., 2001. Fatigue crack propagation in aluminium alloy foams. International Journal of Fatigue 23, 375–382.

Pal, B., Gupta, S., New, A., 2009. A numerical study of failure mechanisms in the cemented resurfaced femur: effects of interface characteristics and bone remodelling. Proceedings of the Institution of Mechanical Engineers, Part H: Journal of Engineering in Medicine 223, 471–484.

Parthasarathy, J., Starly, B., Raman, S., Christensen, A., 2010. Mechanical evaluation of porous titanium (Ti6Al4V) structures with electron beam melting (EBM). Journal of the Mechanical Behavior of Biomedical Materials 3, 249–259.

Peng, L., Bai, J., Zeng, X., Zhou, Y., 2006. Comparison of isotropic and orthotropic material property assignments on femoral finite element models under two loading conditions. Medical Engineering & Physics 28, 227–233.

Pérez, M., Fornells, P., Doblaré, M., García-Aznar, J., 2010. Comparative analysis of bone remodelling models with respect to computerised tomography-based finite element models of bone. Computer Methods in Biomechanics and Biomedical Engineering 13, 71–80.

Pettersen, S.H., Wik, T.S., Skallerud, B., 2009. Subject specific finite element analysis of stress shielding around a cementless femoral stem. Clinical Biomechanics 24, 196–202.

Ploeg, H.-L., Bürgi, M., Wyss, U.P., 2009. Hip stem fatigue test prediction. International Journal of Fatigue 31, 894–905.

Raghavan, P., Ghosh, S., 2004. Concurrent multi-scale analysis of elastic composites by a multi-level computational model. Computer methods in applied mechanics and engineering 193, 497–538.

Raimondi, M., Pietrabissa, R., 1999. Modelling evaluation of the testing condition influence on the maximum stress induced in a hip prosthesis during ISO 7206 fatigue testing. Medical Engineering & Physics 21, 353–359.

Reilly, G.C., Engler, A.J., 2010. Intrinsic extracellular matrix properties regulate stem cell differentiation. Journal of Biomechanics 43, 55–62.

Rodrigues, H., Guedes, J., Bendsoe, M., 2002. Hierarchical optimization of material and structure. Structural and Multidisciplinary Optimization 24, 1–10.

Schuh, A., Bigoney, J., Hönle, W., Zeiler, G., Holzwarth, U., Forst, R., 2007. Second generation (low modulus) titanium alloys in total hip arthroplasty. Materialwissenschaft und Werkstofftechnik 38, 1003–1007.

Senalp, A.Z., Kayabasi, O., Kurtaran, H., 2007. Static, dynamic and fatigue behavior of newly designed stem shapes for hip prosthesis using finite element analysis. Materials & Design 28, 1577–1583.

Sevilla, P., Aparicio, C., Planell, J.A., Gil, F.J., 2007. Comparison of the mechanical properties between tantalum and nickel–titanium foams implant materials for bone ingrowth applications. Journal of Alloys and Compounds 439, 67–73.

Simone, A., Gibson, L., 1998. Effects of solid distribution on the stiffness and strength of metallic foams. Acta Materialia 46, 2139–2150.

Suzuki, K., Kikuchi, N., 1991. A homogenization method for shape and topology optimization. Computer Methods in Applied Mechanics and Engineering 93, 291–318.

Takano, N., Fukasawa, K., Nishiyabu, K., 2010. Structural strength prediction for porous titanium based on micro-stress concentration by micro-CT image-based multiscale simulation. International Journal of Mechanical Sciences 52, 229–235.

Takano, N., Okuno, Y., 2004. Three-scale finite element analysis of heterogeneous media by asymptotic homogenization and mesh superposition methods. International Journal of Solids and Structures 41, 4121–4135.

Takano, N., Zako, M., Ishizono, M., 2000. Multi-scale computational method for elastic bodies with global and local heterogeneity. Journal of Computer-Aided Materials Design 7, 111–132.

Takano, N., Zako, M., Okuno, Y., 2003. Multi-scale finite element analysis of porous materials and components by asymptotic homogenization theory and enhanced mesh superposition method. Modelling and Simulation in Materials Science and Engineering 11, 137–156.

Van Bael, S., Chai, Y.C., Truscello, S., Moesen, M., Kerckhofs, G., Van Oosterwyck, H., Kruth, J.P., Schrooten, J., 2012. The effect of pore geometry on the in vitro biological behavior of human periosteum-derived cells seeded on selective laser-melted Ti6Al4V bone scaffolds. Acta Biomaterialia 8, 2824–2834.

Viceconti, M., Brusi, G., Pancanti, A., Cristofolini, L., 2006. Primary stability of an anatomical cementless hip stem: a statistical analysis. Journal of Biomechanics 39, 1169–1179.

Viceconti, M., Monti, L., Muccini, R., Bernakiewicz, M., Toni, A., 2001. Even a thin layer of soft tissue may compromise the primary stability of cementless hip stems. Clinical Biomechanics 16, 765–775.

Viceconti, M., Muccini, R., Bernakiewicz, M., Baleani, M., Cristofolini, L., 2000. Large-sliding contact elements accurately predict levels of bone-implant micromotion relevant to osseointegration. Journal of Biomechanics 33, 1611–1618.

Vigliotti, A., Pasini, D., 2012. Stiffness and strength of tridimensional periodic lattices. Computer Methods in Applied Mechanics and Engineering 229–232, 27–43.

Wang, A., McDowell, D., 2004. In-plane stiffness and yield strength of periodic metal honeycombs. Journal of Engineering Materials and Technology 126, 137–156.

Weinans, H., Huiskes, R., Grootenboer, H., 1992a. Effects of material properties of femoral hip components on bone remodeling. Journal of Orthopaedic Research 10, 845–853.

Weinans, H., Huiskes, R., Grootenboer, H., 1994. Effects of fit and bonding characteristics of femoral stems on adaptive bone remodeling. Transactions of the ASME-K-Journal of Biomechanical Engineering 116, 393–400.

Weinans, H., Huiskes, R., Grootenboer, H.J., 1992b. The behavior of adaptive bone-remodeling simulation models. Journal of Biomechanics 25, 1425–1441.

Yuan, F., Pagano, N., 2003. Size scales for accurate homogenization in the presence of severe stress gradients. Mechanics of Advanced Materials and Structures 10, 353–365.

Yushkevich, P.A., Piven, J., Hazlett, H.C., Smith, R.G., Ho, S., Gee, J.C., Gerig, G., 2006. User-guided 3D active contour segmentation of anatomical structures: significantly improved efficiency and reliability. Neuroimage 31, 1116–1128.

Zannoni, C., Mantovani, R., Viceconti, M., 1999. Material properties assignment to finite element models of bone structures: a new method. Medical Engineering & Physics 20, 735–740.

Zardiackas, L.D., Parsell, D.E., Dillon, L.D., Mitchell, D.W., Nunnery, L.A., Poggie, R, 2001. Structure, metallurgy, and mechanical properties of a porous tantalum foam. Journal of Biomedical Materials Research 58, 180–187.

Zhou, J., Soboyejo, W.O., 2004. Compression–compression fatigue of open cell aluminum foams: macro-/micro-mechanisms and the effects of heat treatment. Materials Science and Engineering A 369, 23–35.

Zienkiewicz, O.C., Taylor, R.L., 2005. The Finite Element Method for Solid and Structural Mechanics. Butterworth-Heinemann, Burlington, US.